We are IntechOpen,
the world's leading publisher of
Open Access books
Built by scientists, for scientists

6,900
Open access books available

186,000
International authors and editors

200M
Downloads

154
Countries delivered to

Our authors are among the

TOP 1%
most cited scientists

12.2%
Contributors from top 500 universities

Interested in publishing with us?
Contact book.department@intechopen.com

Numbers displayed above are based on latest data collected.
For more information visit www.intechopen.com

An Overview of Densification, Microstructure and Mechanical Property of Additively Manufactured Ti-6Al-4V — Comparison among Selective Laser Melting, Electron Beam Melting, Laser Metal Deposition and Selective Laser Sintering, and with Conventional Powder Metallurgy

Ming Yan and Peng Yu

Additional information is available at the end of the chapter

1. Introduction

Additive manufacturing (AM) is the newest powder metallurgy (PM) technique [1-3] while Ti-6Al-4V is the single most important Ti alloy [4-9]. AM Ti-6Al-4V is being widely pursed by research community and industry for its capability to produce complicated, net-shape engineering parts and/or customised, biomedical implants.

This chapter begins with an introduction of the fundamental properties of Ti-6Al-4V, and its densification mechanism, typical microstructure and mechanical property achievable by conventional PM routes. This functions as a point of reference for the following discussion of the AM Ti-6Al-4V in terms of densification, microstructure, and mechanical property. The mostly popular laser-based AM techniques, namely selective laser melting (SLM), electron beam melting (EBM), laser metal deposition (LMD) and selective laser sintering (SLS), for the fabrication of Ti-6Al-4V have been overviewed based on an analysis of over 100 individual studies. Heat treatment is essential to most of the AM Ti-6Al-4V. Principles for selecting appropriate heat treatment for the AM Ti-6Al-4V are proposed based on martensite phase transformation and optimisation of mechanical properties. Oxygen impurity is an issue to most Ti materials and it is addressed in this chapter as well; counter measurements to mitigate oxygen have been suggested which involves the use of rare earth based materials.

INTECH
open science | open minds

2. Preliminary knowledge: Fundamental properties of Ti-6Al-4V and conventional PM Ti-6Al-4V

2.1. Densification of PM Ti-6Al-4V and typical microstructure and mechanical property

- **Sintering mechanism:** Sintering/densification of conventional PM Ti-6Al-4V is mostly through solid state sintering. Sintering temperatures are normally selected in the β phase region [10-13], at a temperature (e.g. at 1300ºC) well below the liquidus temperature (~1660 ºC for Ti-6Al-4V, Table 1) [14,15]. For sintering under pressure such as via hot pressing or spark plasma sintering, the sintering temperature can be lower, for instance, around 900°C [16]. Driving force for densification during solid state sintering is reduction of surface area and surface free energy by eliminating solid-vapour interfaces [17-19]. Sintering procedure mainly involves diffusional flow of composing elements, including surface diffusion, grain boundary diffusion and lattice diffusion [17-19].

- **Sintering activation energy:** Using the master sintering curve approach, Crosby [20] estimated that sintering activation energy, the Q value, of Ti-6Al-4V is about 130 kJ/mole. This is consistent with the reported Q value of the self-diffusion of titanium (92.5 kJ/mole-158 kJ/mole) over the β-Ti range from 900 to 1250 ºC, affirming that the densification of Ti-6Al-4V is mainly controlled by self-diffusion of titanium [8].

- **Sintered density:** Most of the as-sintered Ti-6Al-4V materials show 95%-99% of theoretical density [4-13]. The as-sintered density depends on a few factors such as compaction pressure and powder size. Using TiH_2 as the starting powder may assist in improving the as-sintered density [21,22], but to achieve a pore-free alloy (no less than 99.8% of theoretical density) post treatment such as via extrusion or hot isostatic pressing (HIP) is necessary [23].

- **Microstructure of PM Ti-6Al-4V**: PM Ti-6Al-4V is expected to show the following microstructural characteristics [24]: (a) The overall microstructure is close to the equilibrium state due to low cooling rate adopted for most sintering practices. (b) There could be some annealing and/or aging effect resulting from the slow cooling process from the isothermal sintering temperature to room temperature. Aging-induced phases such as isothermal ω may form during cooling. (c) Pores are part of the as-sintered microstructure due to the difficulty to achieve a pore-free microstructure in most cases. Fig. 1(a) provides a typical SEM image of the as-sintered PM Ti-6Al-4V, consisting of grain boundary α, α lath and β phases [25]; the overall volume fraction of the α phase is more than 85% [10-13].

- **Mechanical property of PM Ti-6Al-4V:** Mechanical properties of the PM Ti-6Al-4V are highly dependent upon oxygen level. Typical cases are shown in Figure 1(b) to demonstrate ductility of PM Ti-6Al-4V as a function of oxygen [26]. The fracture strength of PM Ti-6Al-4V is comparable or even higher than the wrought material (ASTM B348) [9].
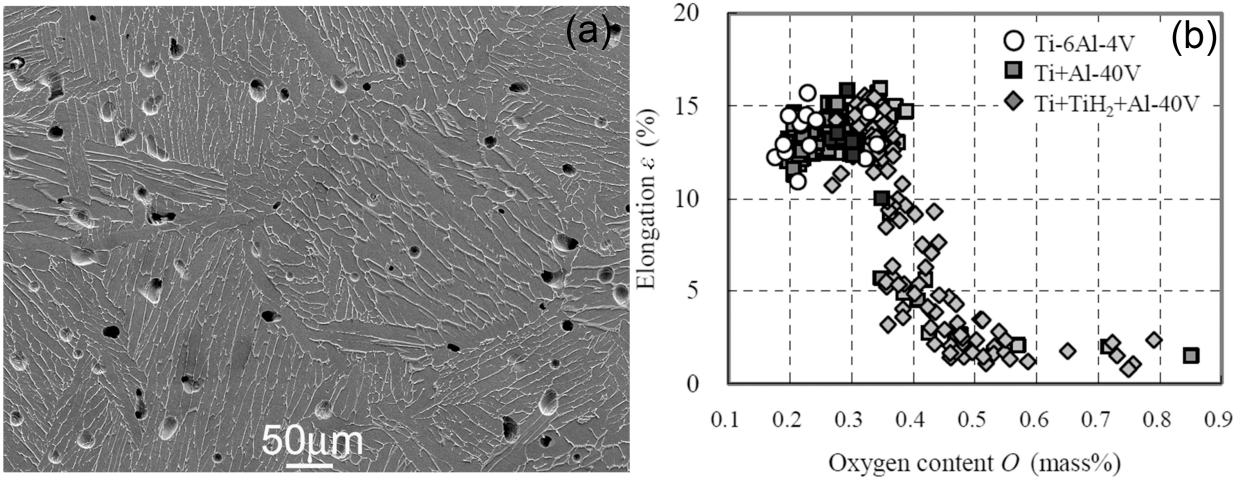
Figure 1. (a) Scanning electron microscopy (SEM) image to show the typical microstructure of PM Ti-6Al-4V [25] and (b) ductility of PM Ti-6Al-4V as a function of oxygen [26].

2.2. Ti-6Al-4V: Basic physical and mechanical properties

Table 1 and Table 2 list the fundamental physical and mechanical properties of the Ti-6Al-4V, respectively [14,15,27,28]. They serve as a point of reference and provide benchmark values for the following discussion on the AM Ti-6Al-4V.

Physical property	Value
Density of solid (ρ)	4.43 g/cm^3
Density of liquid (ρ)	3.89 g/cm^3
Solidus temperature	1877 K (1604°C)
Liqudus temperature	1933 K (1660°C)
Temperature of (α+β) → β	1253K (980°C)
Temperature of α → β	~1023K (750°C)
Thermal conductivity of solid (k_s)	6.7 W/m/K
Thermal conductivity of liquid (k_l)	32.5 W/m/K
Specific heat capacity of solid (Cp_s)	0.526 J/g/K
Specific heat capacity of liquid (Cp_l)	0.872 J/g/K
Coefficient of thermal expansion of solid (K^{-1})	8.6 μm/m/K
Temperature of martensite phase transformation (M_s)	~1053K (780°C) or ~883K(610°C)

Table 1. Fundamental physical properties of Ti-6Al-4V [14,15,27,28]

Mechanical property	Value
Tensile strength, yield ($\sigma_{0.2}$)	880 MPa
Tensile strength, Ultimate (UTS)	950 MPa
Elongation (ε)	14 %
Reduction of Area (R)	36%
Hardness, Hv	349
Young's modulus (E)	113.8 GPa
Poisson's ratio (v)	0.342
Fatigue strength (at $1*10^7$ cycles and K = 3.3)	240 MPa
Fatigue strength (unnotched at $1*10^7$ cycles)	510 MPa
Fracture toughness	75 MPa•m$^{1/2}$

Table 2. Mechanical properties of Ti-6Al-4V achievable via forged- then-annealed [14,15,27,28]

3. Various AM approaches for Ti-6Al-4V and their key processing parameters

3.1. Selective Laser Melting (SLM)

There are a variety of suppliers providing reliable SLM machines for producing AM Ti-6Al-4V [29-46]. EOSINT M270, Trumpf LF250, and SLM Solutions are well known SLM facilities. Figure 2 shows a schematic graph to present the working principle of the SLM [46]. Table 3 provides a summary about the key machine parameters and working conditions via a typical SLM machine, SLM 280 HL [29-46].

	Parameter
Typical equipment	SLM 280HL
Build volume	280 mm * 280 mm * 350 mm
Laser type	YLR Fibre Laser
Laser beam size	70 μm - 120 μm
Atmosphere during processing	With protection by Ar, N_2 or He
Scanning speed	Up to 15000 mm/s (mostly 125 mm/s – 802 mm/s)
Feed type	5 μm – 50 μm
Layer thickness	Mostly 20 μm – 75 μm
Build temperature	Mostly naturally heated
Build density	99.7% - 100%
Substrate	Without substrate; or with self-substrate heated up to 700°C

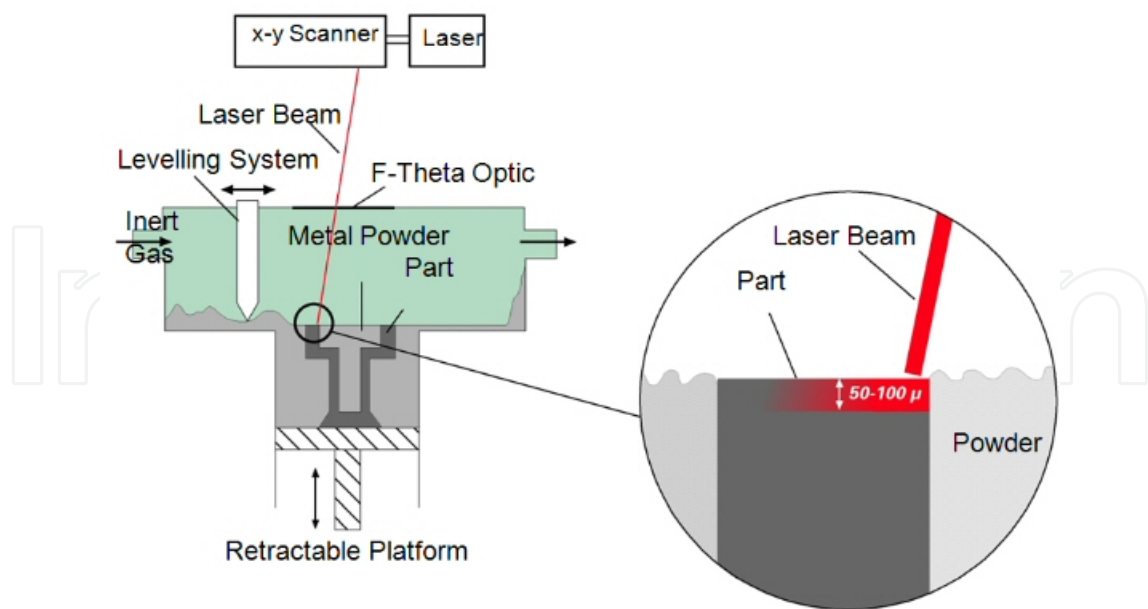**Table 3.** Typical technical parameters of the SLM [29-46].

Figure 2. Schematic graph to show the working principle of the SLM [46].
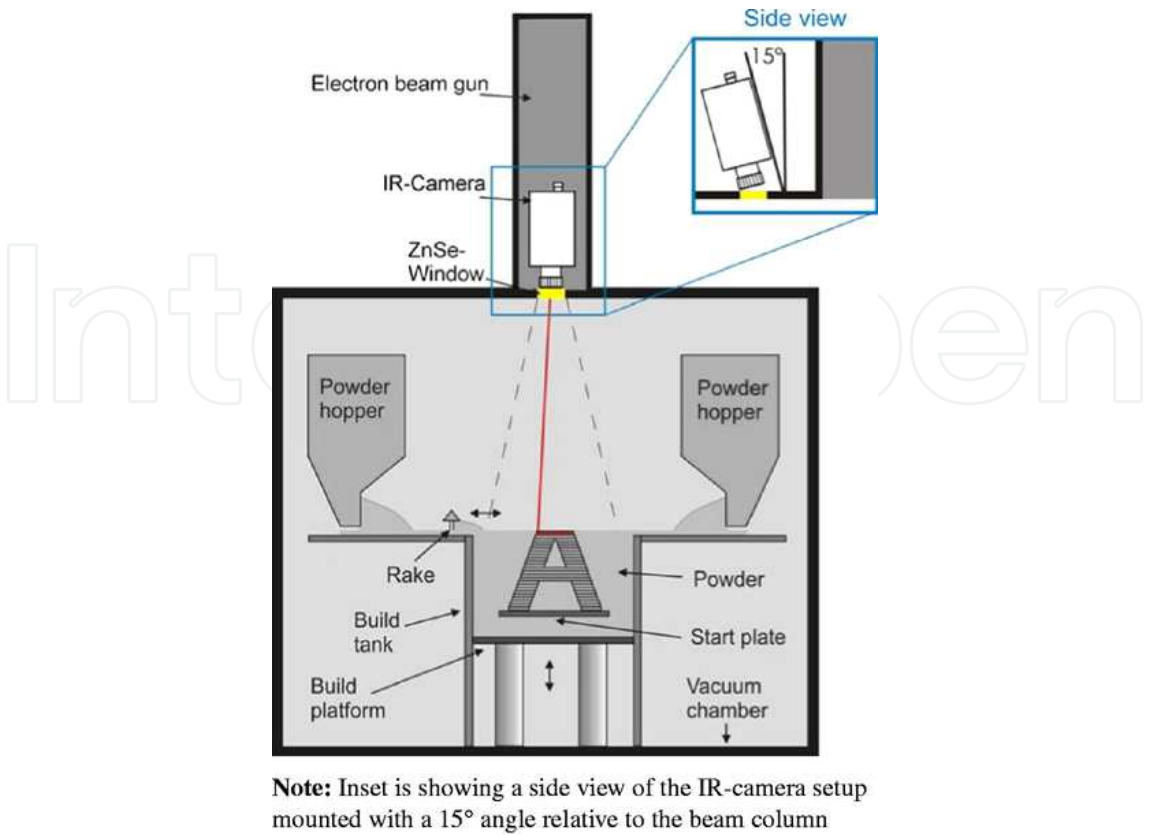
3.2. Electron Beam Melting (EBM)

Arcam provides a variety of EBM machines for processing Ti and Ti alloys, including Arcam A1, A2, S12 and S400, and it dominates the market for the time being [47-66]. Figure 3 provides a schematic graph to show the working principle of the EBM [66]; key machine parameters and working conditions are summarised into Table 4 via a typical example of Arcam A2 EBM.

	Parameter
Typical equipment	Arcam A2
Build volume	250 mm * 250 mm * 400 mm or Φ300 mm * 200 mm
Powder supply	7 kW max.
Laser beam size	200 μm – 1000 μm (mostly 100 μm - 500 μm)
Atmosphere during processing	10^{-1} Pa - 10^{-3} Pa, or with protection by partial pressure of He
Scanning speed	Up to 8000 mm/s (mostly 125 mm/s – 802 mm/s)
Feed type	25 μm – 149 μm (40μm - 100μm standard)
Layer thickness	20 μm – 100 μm
Build temperature	640°C - 700°C
Build density	99.4% - 100%
Substrate	Stainless steel, normally heated to 720°C - 800°C

Table 4. Typical technical parameters of the EBM [47-66].

Note: Inset is showing a side view of the IR-camera setup mounted with a 15° angle relative to the beam column
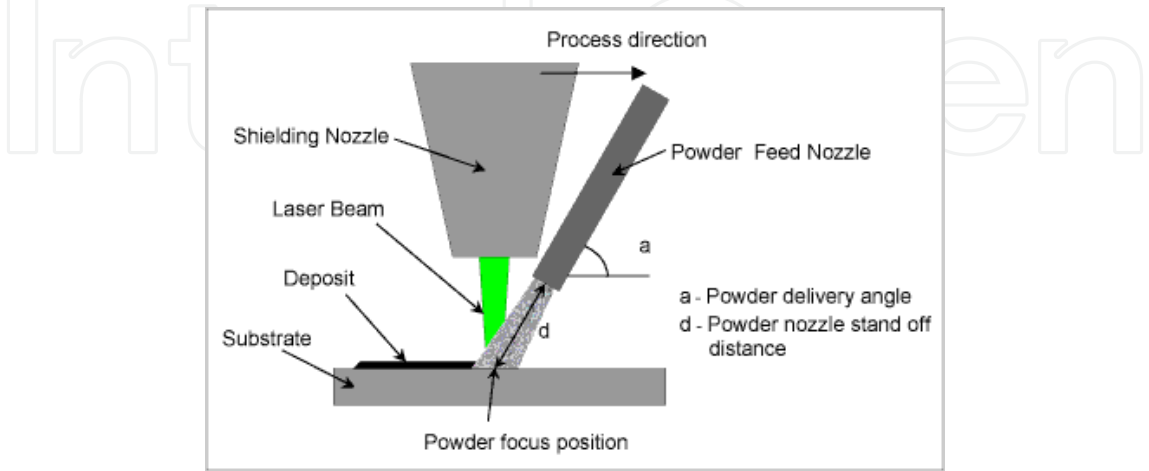
Figure 3. Schematic graph to show the working principle of an EBM equipment [66].

3.3. Laser Metal Deposition (LMD)

A variety of LMD machines and laser systems are being used for the fabrication of metals and alloys including Ti-6Al-4V, such as LEMS TM Nd:YAG, Trumpf HLD 3504 Yb:YAG and IPG with Yb fibre laser [67-78]. Figure 4 and Table 5 present the general working principle, working conditions and key machine/processing parameters.

Figure 4. Schematic graph to show the working principle of an LMD equipment [76].

	Parameter
Typical equipment	Trumpf HLD 3504
Build volume	250 mm* 250 mm * 400 mm
Powder supply	3.5 kW max.
Laser beam size	Mostly 500 μm - 4100 μm
Atmosphere during processing	Argon flow protection
Scanning speed	Mostly 2 mm/s – 40 mm/s
Feed type	Mostly 10 μm – 200 μm (powder); 1.2 mm - 1.6 mm wire
Layer thickness	40 μm – 100 μm
Build temperature	Naturally heated
Build density	Can be >99.9%
Substrate	Ti-6Al-4V or Ti; room temperature or preheated to 200°C

Table 5. Typical technical parameters of the LMD [67-76].

3.4. Selective Laser Sintering (SLS)

EOSINT M250X and EOISNT M270 are being used as the SLS machines for preparing AM Ti-6Al-4V [79-88]. The general working conditions and key machine/processing parameters are shown by Figure 5 and listed in Table 6.
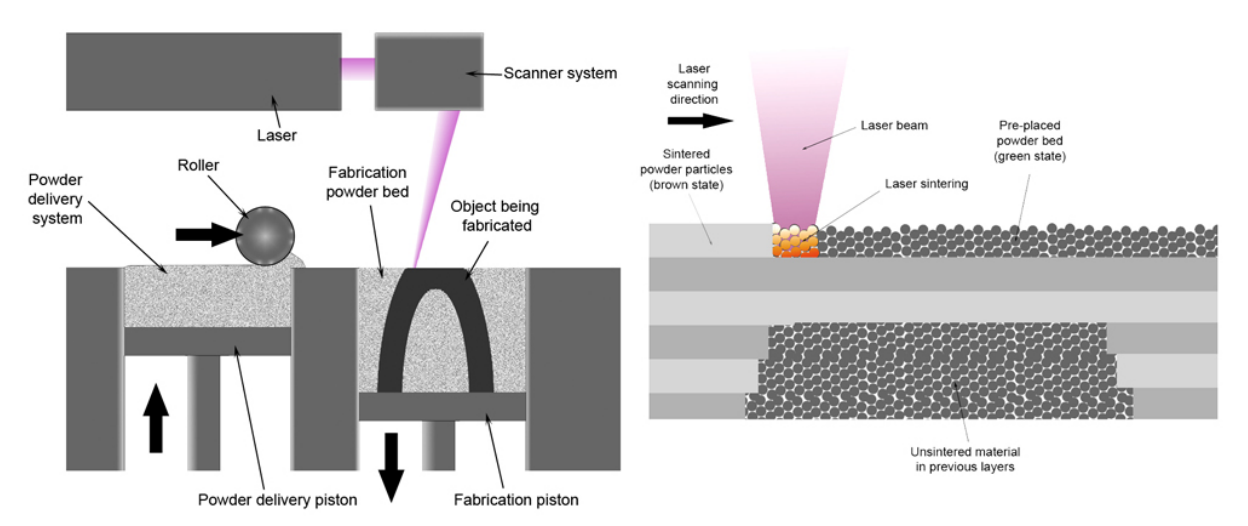

**Figure 5.** Schematic graph to show the working principle of an SLS equipment [88].

	Parameter
Typical equipment	EOSINT M270
Build volume	250 mm * 250 mm * 215 mm
Laser type	Yb-fiber laser, 200 W
Powder supply	5.5 kW max.
Laser beam size	100 μm - 500 μm
Scanning speed	Up to 7000 mm/s (mostly 50 mm/s - 100 mm/s)
Layer thickness	20 μm - 100 μm
Feed type	Mostly 37 μm - 74 μm (should be similar to SLM)
Build temperature	- (can use preheated powder at e.g. 600°C)
Build density	Mostly below 99%
Substrate	Normally Ti, can be heated to e.g. 230 °C

Table 6. Typical technical parameters of the SLS [77-88].

4. Densification of AM Ti-6Al-4V

4.1. As-built density of AM Ti-6Al-4V

Figure 6 summarises reports on as-built density of the AM Ti-6Al-4V using LMD, SLM, EBM, and SLS [29-88]. The figure shows that the as-built density of AM Ti-6Al-4V is mostly higher than 99% of theoretical density and the material can be fully dense if processing parameters are appropriately selected. SLS Ti-6Al-4V is exceptional to this conclusion, which as-built densities are around 95% and similar to the as-sintered density of the conventional PM Ti-6Al-4V [4-13].
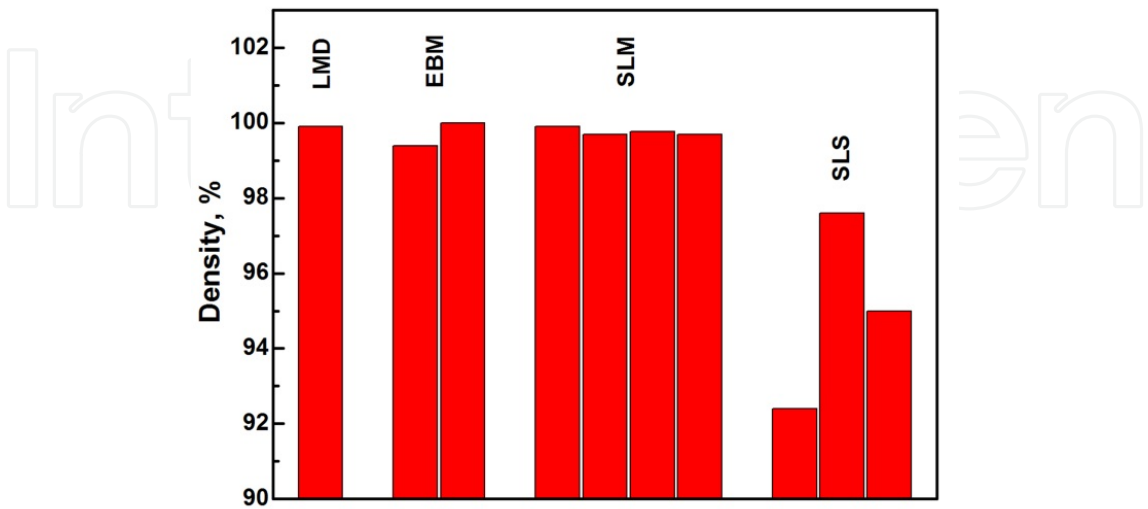

Figure 6. Density of as-built AM Ti-6Al-4V [29-88].

4.2. Densification of SLS Ti-6Al-4V: Solid state sintering and liquid phase sintering

The fact that the as-built density of the SLS Ti-6Al-4V is similar to that of the conventional PM Ti-6Al-4V (see Figure 6) implies the two processing approaches should have analogous densification mechanism. This is understandable by referring to Figure 5 which shows that the SLS processing uses laser as the heating source while for the conventional PM Ti-6Al-4V, heating is mainly through conductive and/or radiation heat. Other than this the two processing pathways are essentially same. This further suggests that the driving force and activation energy for densification of the conventional PM Ti-6Al-4V should be applicable to the SLS Ti-6Al-4V. During SLS of Ti-6Al-4V, however, there is possibility that liquid phase sintering (LPS) occurs due to local overheating to temperatures higher than the liquidus temperature of Ti-6Al-4V (~1660°C). LPS provides extra driving force for sintering for it has extra surface energies, i.e. resulted from liquid surface and from liquid-solid interface [89,90]. It involves different sintering mechanisms, e.g. pore-filling, from the solid state sintering. These normally can contribute to an as-sintered density of up to 99.5% high [89,90]. Since the as-sintered density of the SLS Ti-6Al-4V is lower than this value, the overwhelming densification mechanism for the SLS Ti-6Al-4V should still remain as that of the solid state sintering.

4.3. Densification of EBM, SLM, and LMD Ti-6Al-4V: Solidification from liquid

Full or nearly full denseness is achievable in EBM, SLM and LMD Ti-6Al-4V (see Figure 6), implying that the densification mechanism for these AM approaches is different from that of
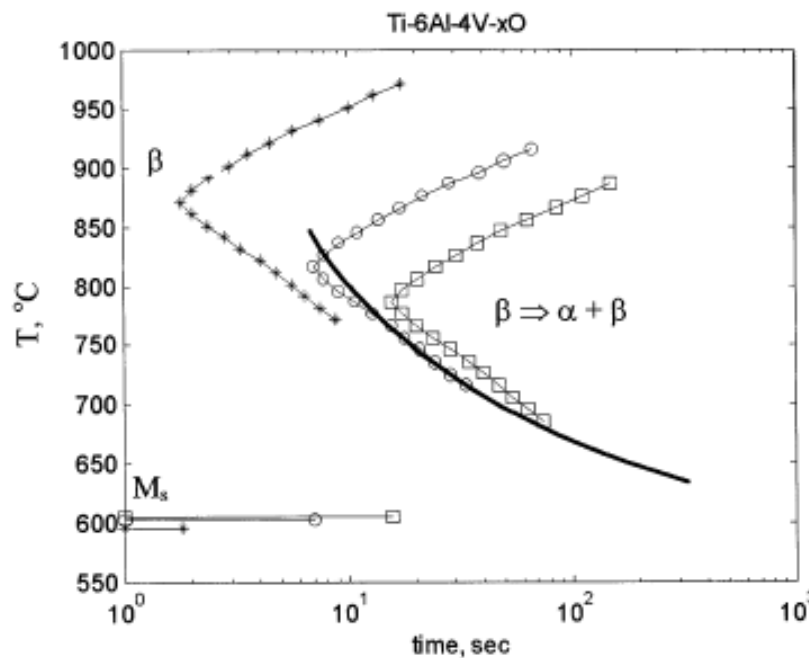

Figure 7. Simulated T-T-T curve of Ti-6Al-4V, which can be used to forecast the phase selection during solidification of the alloy [91]. M_s in the figure denotes the martensite phase transformation. Open squares in the figure are for 0.05wt. %O, circles for 0.1 wt.% and stars for 0.2 wt.%O. The solid line is drafted based on experimental results. Oxygen (O) is found to be able to lower the temperature for the martensite phase transformation.

the SLS. Indeed, for these three laser-based processing approaches, the densification process is more of solidification from liquid rather than the normal sense of sintering. The so-called time-temperature-transformation (T-T-T) of Ti-6Al-4V regulates phase selection and phase constitution of the solidified microstructure. Figure 7 provides the T-T-T curve of the Ti-6Al-4V alloy containing different levels of oxygen [91]. Under equilibrium conditions (i.e. low cooling rates), the resultant microstructure will be a mixture of thermodynamically stable α and β phases, while high cooling rates can enable formation of martensite phases.

5. Microstructure of AM Ti-6Al-4V (As built)

5.1. Microstructure of SLS Ti-6Al-4V

SLS is largely similar to the conventional PM and this explains that the microstructure of SLS Ti-6Al-4V is close to that of equilibrium state as with the PM or cast Ti-6Al-4V [79-88]. Figure 8 compares the microstructure of SLS Ti-6Al-4V with that of an HIP Ti-6Al-4V [81]. In general both materials are of lamellar structure consisting of (α+β) phases and show no evident difference to each other.
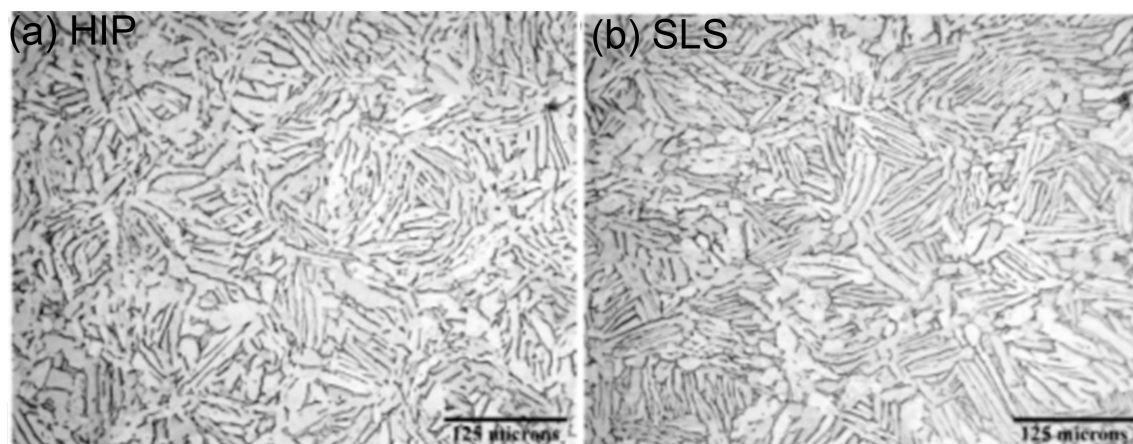
Figure 8. Optical microscopy images of (a) an HIP Ti-6Al-4V and (b) an SLS then HIP Ti-6Al-4V. The latter generally presents a lamellar type of microstructure and almost identical to the former [81].

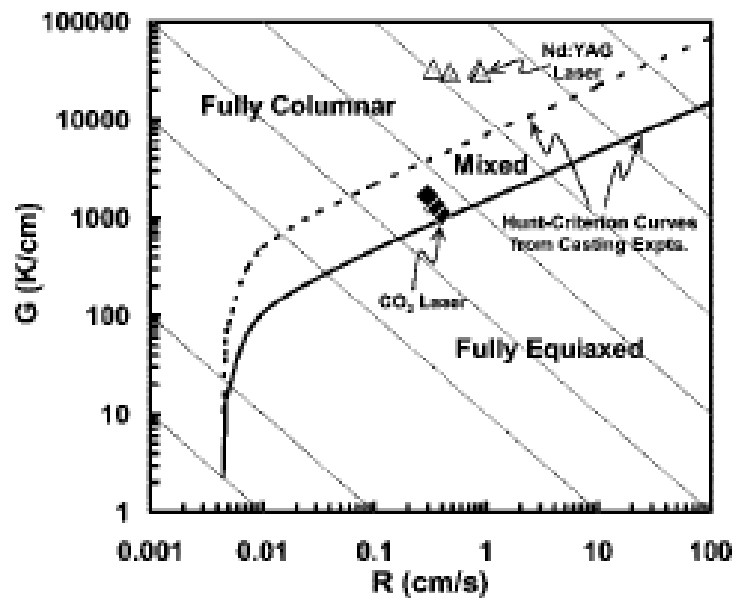### 5.2. Microstructure of EBM, SLM and SMD Ti-6Al-4V

5.2.1. Solidification map

As aforementioned, regarding EBM, SLM and SMD, the AM processing is essentially a solidification process [29-78]. In this regard, the solidification map (see Fig. 9) suggested by Kobryn and Semiatin [1] is useful for predicting the solidification microstructure and can even be served for microstructural design. The two parameters, R and G, that are crucial for composing the solidification map can be measured and/or calculated as follows:

$$R = \mathrm{d}z \,/\, \mathrm{d}t \tag{1}$$

$$G = \mathrm{d}T \,/\, \mathrm{d}z \tag{2}$$

where R is the solidification velocity which can be calculated based on a distance ($\mathrm{d}z$) moved by solidus isotherm over a certain amount of time ($\mathrm{d}t$), and G is the thermal gradient which can be obtained using a temperature window ($\mathrm{d}T$) between solidus and liquids isotherms over a certain amount of distance ($\mathrm{d}z$).

**Figure 9.** Solidification map of Ti-6Al-4V with simulated laser-glaze data points [1].

5.2.2. Texture and heterogeneity issue

Texture and heterogeneity are widely observable microstructural features in EBM, SLM and SMD Ti-6Al-4V [29-76]. They are formed mainly due to the following two reasons: (a) different temperature distribution in the as-built sample and (b) different cooling rates in the various parts of the sample.

Figure 10 provides optical graphs for an EBM Ti-6Al-4V at the transverse direction (Fig. 10a) and longitudinal direction (Fig. 10b) [4]. The former shows a lamellar microstructure while the later presents directional growth along the build direction. Greater thermal gradient in the latter is suggested to be the main reason for the formation of this columnar type of micro-structure [4]. Figure 11 shows other two examples to illustrate the microstructural heteroge-neity between the surface (Fig. 11a) and the bulk material (Fig. 11b) [71]. In this case, the much faster cooling rate in the surface of the AM Ti-6Al-4V has contributed to the formation of the

acicular, metastable martensite phases in Fig. 11(a) while the bulk material presents a bimodal, equilibrium microstructure due to a much lower cooling rate, see Fig.11(b).
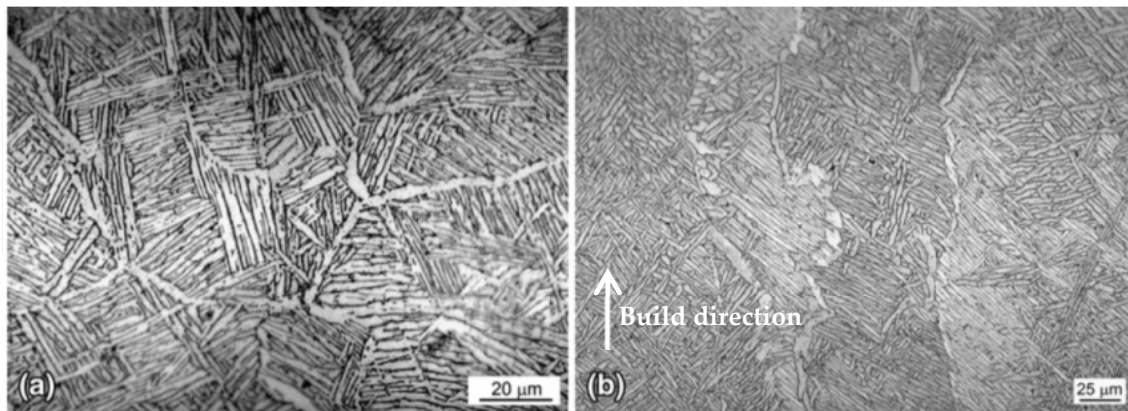
Figure 10. Optical microscopy images of the EBM Ti-6Al-4V from the (a) transverse cross-section and (b) longitudinal cross-section. Build direction is given in (b). Texture/directional growth can be found in (b) [4].
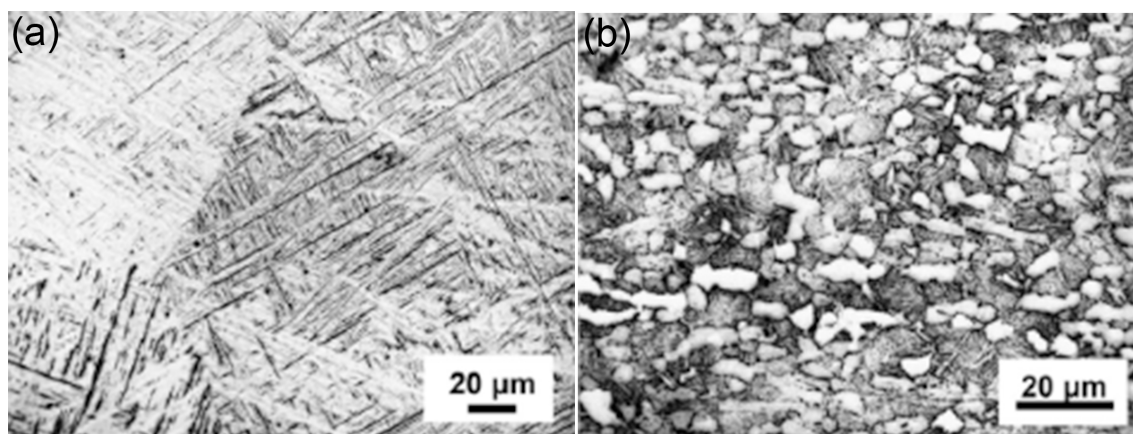

Figure 11. SEM images of the LMD Ti-6Al-4V which show heterogeneity among (a) the surface of the alloy (lamellar with martensite phases) and (b) base/bulk material [71].

5.2.3. Martensite phase transformation

Cooling rate of SLM, EBM and LMD can be 10^4 K/s-10^6 K/s high [29-76]. This enables martensite phases to form in the microstructure. Figure 12 proposes the dependency of phase selection on the cooling rate for Ti-6Al-4V [92,93]. Acicular α, massive martensite α_m or equilibrium (α +β) is proposed for each representative cooling rate. A minimum cooling rate of 20°C/s is suggested to be necessary for the formation of the martensite phases while when cooling rate is higher than 525°C/s the entire microstructure can be featured as acicular α martensite. One still needs to note that the real cooling rate during AM processing of Ti-6Al-4V, other materials as well, is still a research question to be further investigated. Figure 13 provides an example from an EBM Ti-6Al-4V where featherless α can be found in the microstructure [94]. The stable

α phase is also observable in the microstructure although it is suggested that the cooling rate during EBM can be much higher than the critical cooling rate for the martensite phase transformation and accordingly the microstructure should have been overwhelmingly martensite. This is not consistent with the microstructural observation.
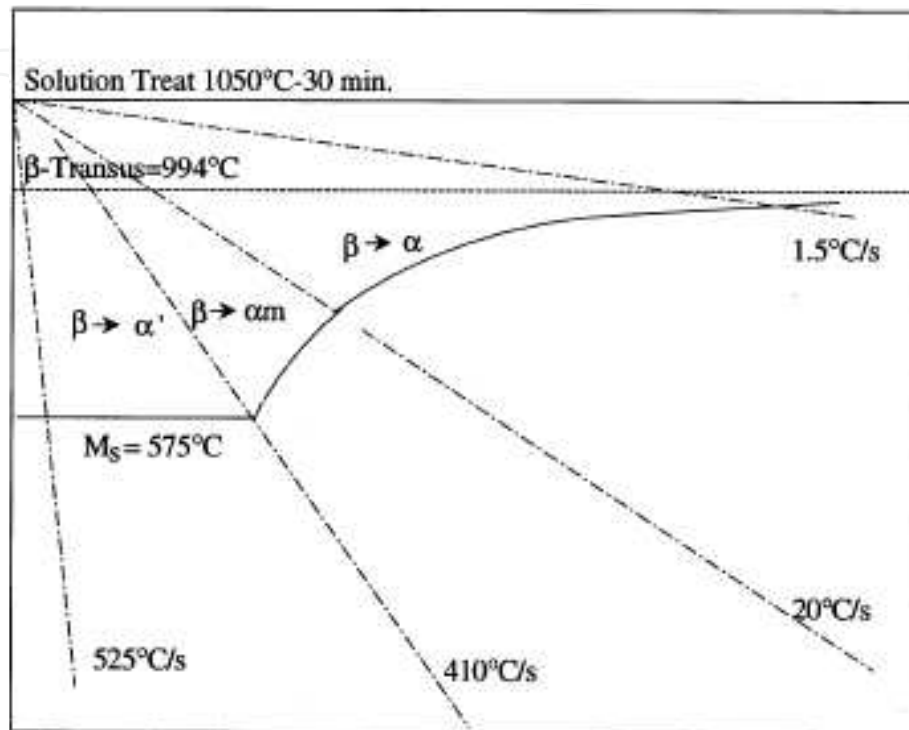
Figure 12. Schematic graph to show the relationship between phase selection and cooling rate during solidification (from 1050°C). The initial state of the Ti-6Al-4V alloy is as β phase [92,93].
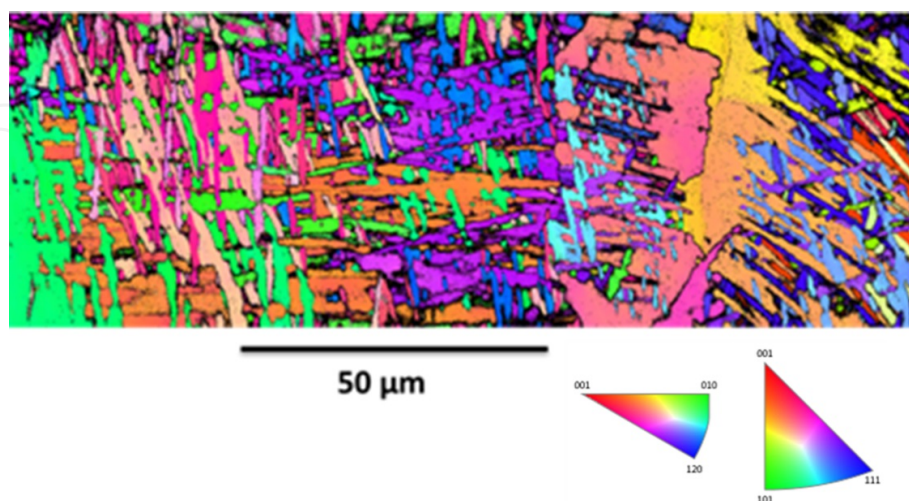

Figure 13. Electron beam scattered diffraction (EBSD) image to show the featureless α' martensite phase and the surrounding microstructure of an EBM Ti-6Al-4V [94].

6. Mechanical property of AM Ti-6Al-4V (As built)

UTS and elongation of as-built AM Ti-6Al-4V are summarised into Figure 14 (a) and (b) [29-88]. ASTM requires that as-prepared Ti-6Al-4V should be no lower than 860 MPa in UTS and no lower than 10% in elongation. These two benchmark values are marked in the two figures using dotted lines. These data suggest that, comparatively speaking, EBM is able to provide a combination of good facture strength and good ductility which satisfy the ASTM specifications. Ti-6Al-4V made by SLM tends to show the highest fracture strength among the four AM approaches yet the corresponding ductility is the lowest which is mostly below the corresponding benchmark value (10%). There are no adequate data for LMD but it is reckoned that it should show a similar tendency to that of the SLM due to the similarity between the two processing techniques. Because of poor density (see Figure 6), SLS Ti-6Al-4V normally relies on post treatment such as HIP to achieve good fracture strength as well as ductility.
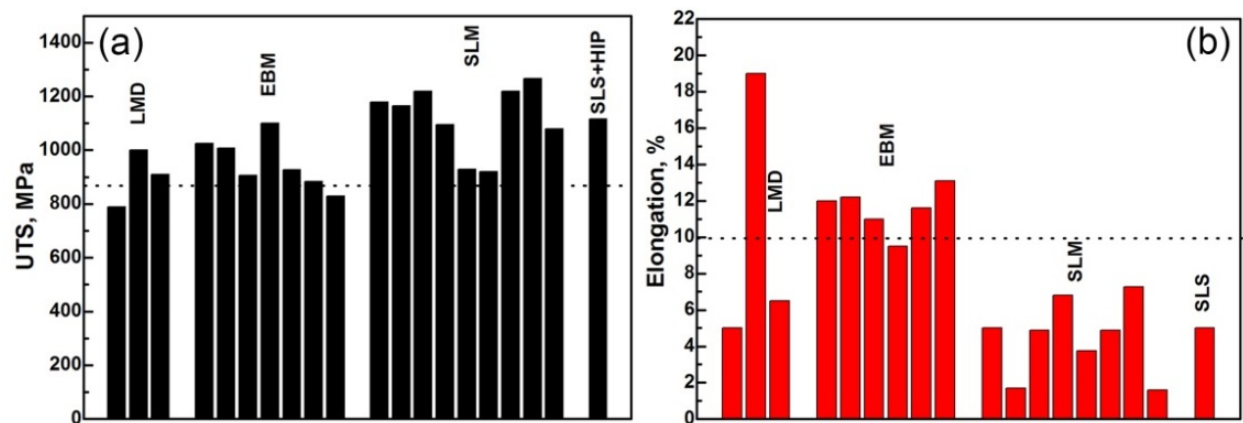

Figure 14. (a) UTS and (b) elongation of as-built Ti-6Al-4V prepared by the various AM techniques [29-88]. Dotted lines in the two figures represent corresponding ASTM specifications.

7. Heat treatment of AM Ti-6Al-4V and corresponding microstructure and mechanical properties

7.1. Heat treatment temperature: A collection from AM Ti-6Al-4V and corresponding mechanical property

Results show that the residual stress in AM Ti-6Al-4V can be higher than 1000 MPa [33]. Considering that the yield strength of Ti-6Al-4V is merely around 880 MPa (see Table 2), residual stress can initiate premature failure especially during dynamic testing such as fatigue. It is a major concern for the AM Ti-6Al-4V. Most as-built AM Ti-6Al-4V therefore need heat treatment to mitigate the impact of the residual stress on the mechanical property performance. A collection of heat treatment temperatures being adopted by current studies is shown in Fig. 15 [29-88]. Temperatures of the martensite phase transformation (at ~610°C), $\alpha \to \beta$ (at ~750°C)

and β-transus (at ~980°C) are also marked in the figure using dotted lines. The figure indicates that most of the heat treatments are distributed at temperatures between 610°C and 980°C. This is very likely due to the necessity of eliminating the hard-but-brittle martensite phases via phase transformation from the α' and/or the α_m phases to stable (α and/or β) phases for the LMD, EBM and SLM approaches. The microstructure of the SLS Ti-6Al-4V is similar to that of the equilibrium state, and can be free from any post heat treatment.
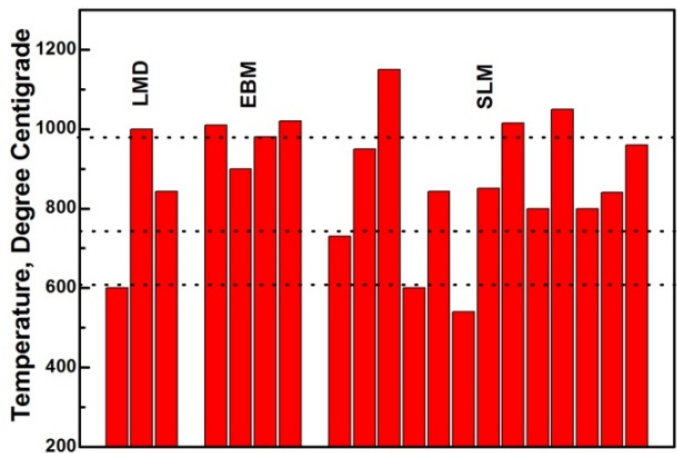
Figure 15. Collection of heat treatment temperatures adopted by various studies of the AM Ti-6Al-4V [29-88]. Dotted lines in the figure represent critical temperatures for Ti-6Al-4V (refer to Table 1).

UTS and elongation of the as-annealed AM Ti-6Al-4V are shown in Fig.16 [29-88]. If comparing with the as-built data (see Fig. 14), the general trend is that the fracture strength will be reduced after heat treatment while ductility can be improved. This is mainly resulted from both the reduced residual stress due to the heat treatment and the partially or even fully transformed martensite phases in the as-built microstructure.
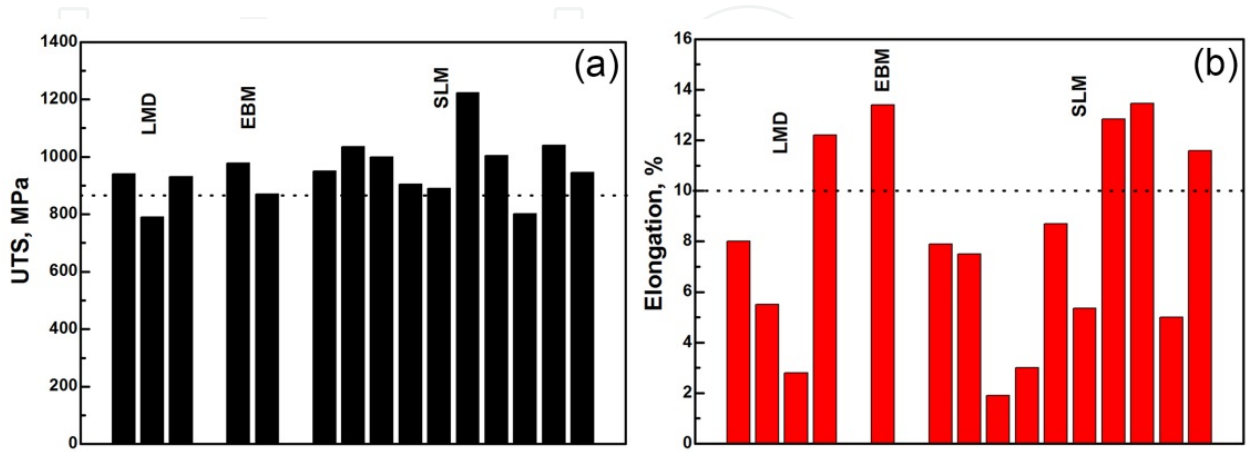
Figure 16. (a) UTS and (b) elongation of as-annealed AM Ti-6Al-4V [29-88]. Dotted lines in the two figures represent corresponding ASTM specifications.

7.2. Stress relief annealing and corresponding microstructure of as-annealed AM Ti-6Al-4V

Heat treatment at temperatures below the temperature of the martensite phase transformation may be not able to change the microstructure. Figure 17 provides such an example via an EBM Ti-6Al-4V annealed at 600°C for four hours [69]. The martensite phases are still observable after the annealing. Such heat treatment may only offer stress relief to reduce the residual stress in the as-built AM Ti-6Al-4V.
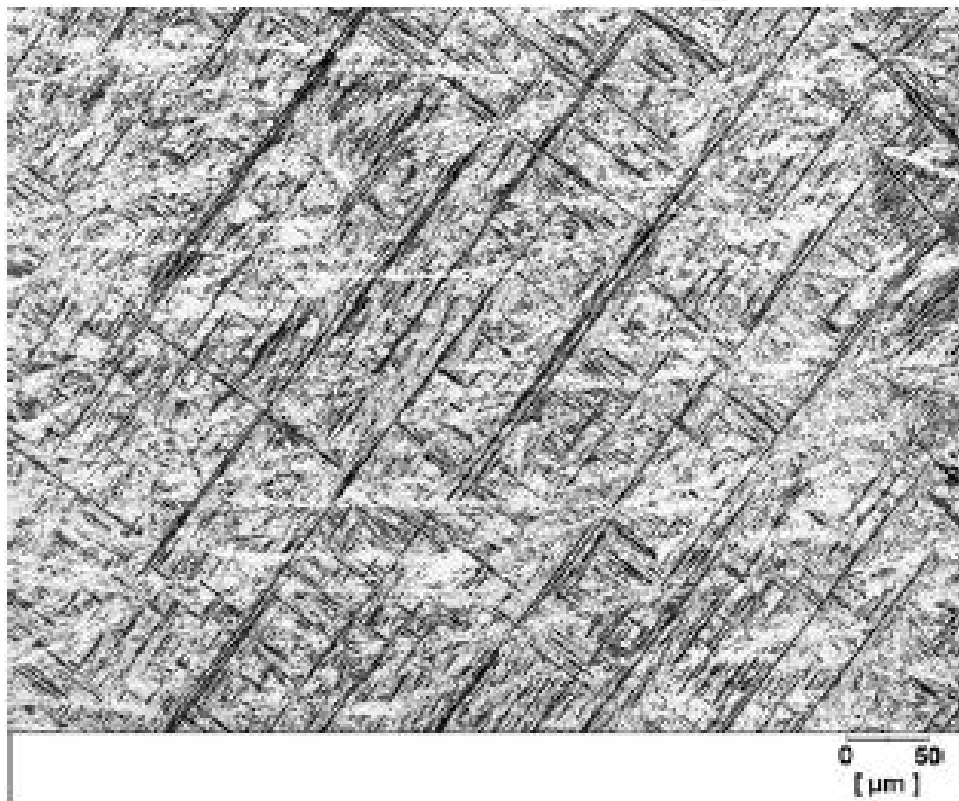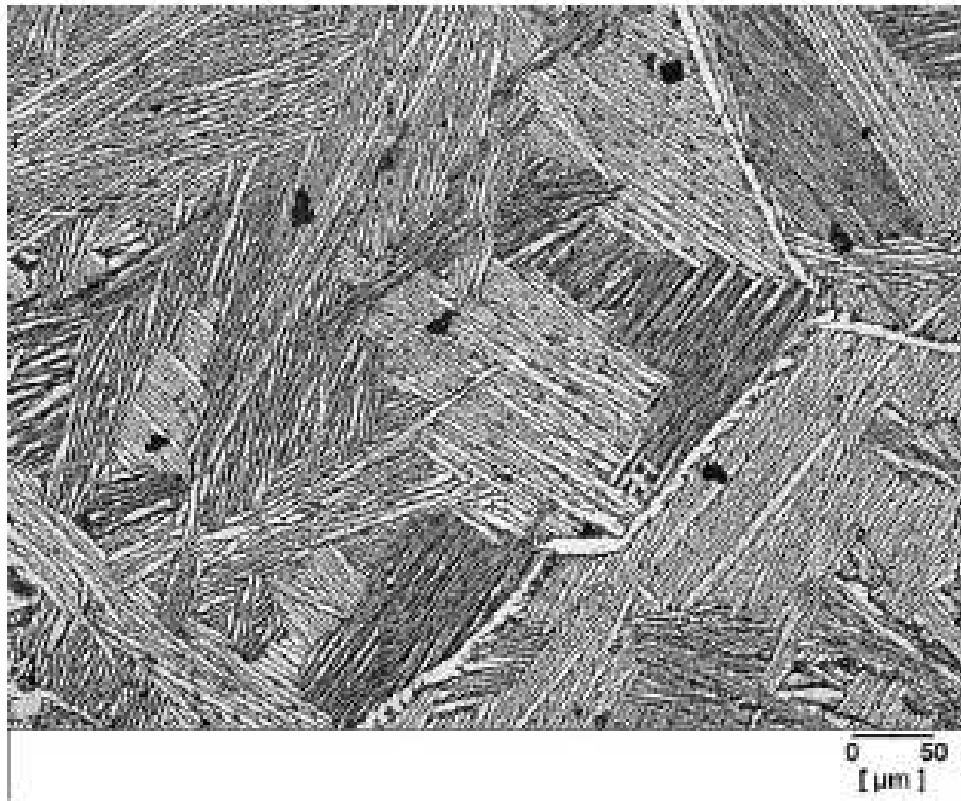

Figure 17. Microstructure of an EBM Ti-6Al-4V annealed at 600°C for four hours. Rectangular (acicular) shaped martensite phases remained after the heat treatment [69].

7.3. Heat treatment to achieve equilibrium microstructure of AM Ti-6Al-4V

7.3.1. Heat treatment at temperature above the martensite phase transformation

Contrary to the low temperature annealing, heat treatment at temperatures higher than the martensite phase transformation may assist in eliminating the brittle, metastable martensite phases via phase transformation [29-88]. Increasing the heat treatment temperature to higher

than the $\alpha \to \beta$ (at ~750°C) or even the β-transus (at ~980°C) will facilitate the transformation from α to β. Figure 18 provides an example of this where heat treatment was conducted up to 1200°C to form equilibrium lamellar (α+β) microstructure [69]. Martensite phases were not observable after such high-temperature heat treatment.


Figure 18. Microstructure of an LMD Ti-6Al-4V annealed at 1200°C for two hours. Colony α-phase is observable along with prior β grains and grain boundary α phases [69].

7.3.2. Dependence of α colony size on heat treatment and microstructural dependency of mechanical property

The model developed by Tiley et al. [95,96] suggests that the mechanical performance of the (α+β) dual phase Ti-6Al-4V can be estimated based on a variety of microstructural parameters including the size of the α colony. The schematic graph in Figure 19 suggests that increasing size of the α colony may lead to reduced ductility (ε) and yield strength ($\sigma_{0.2}$) but in the meantime it may also contribute to better resistance to macro-cracks [95,96]. It is noted that heat treatment can coarsen the α colony of the AM Ti-6Al-4V, see Fig. 20 [54]. From this perspective, heat treatment of AM Ti-6Al-4V will have to be selected according to specific requirement and serve the application purpose of the material.
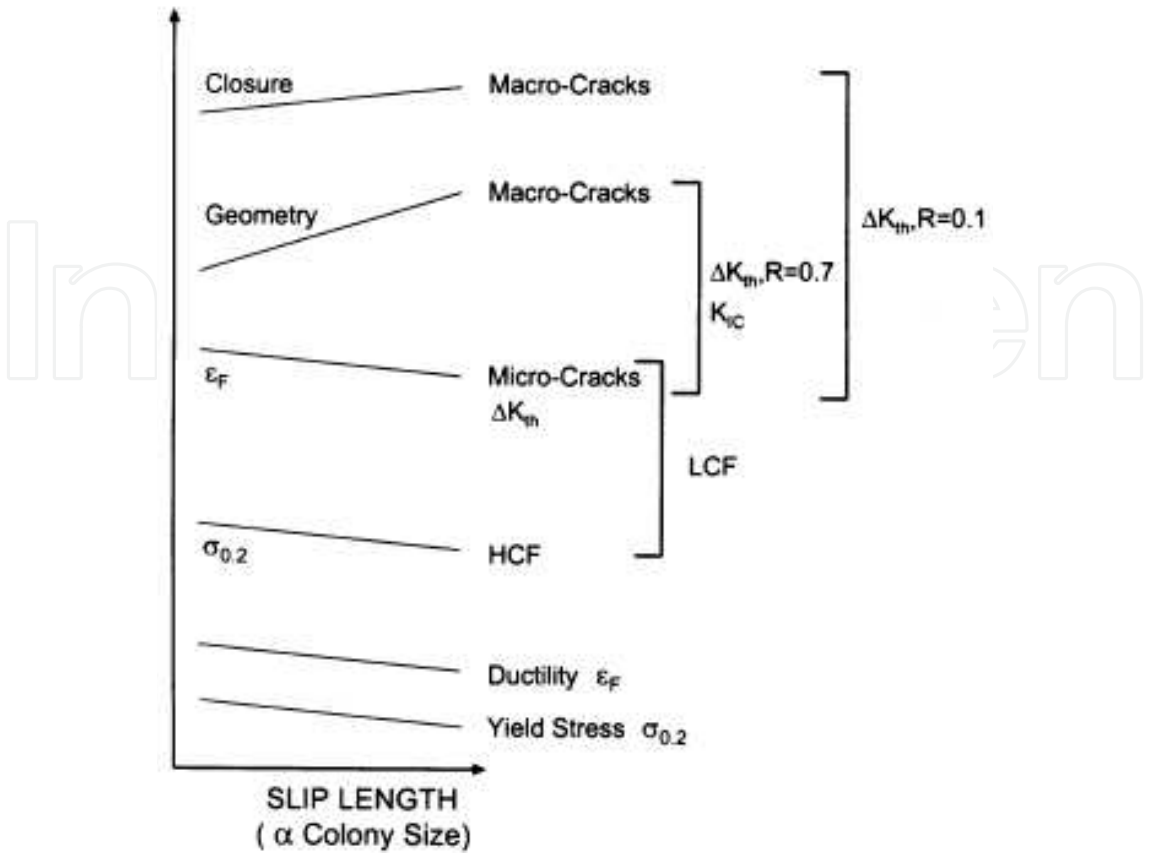
Figure 19. Dependency of mechanical property on the α colony size of the Ti-6Al-4V alloy [95,96].
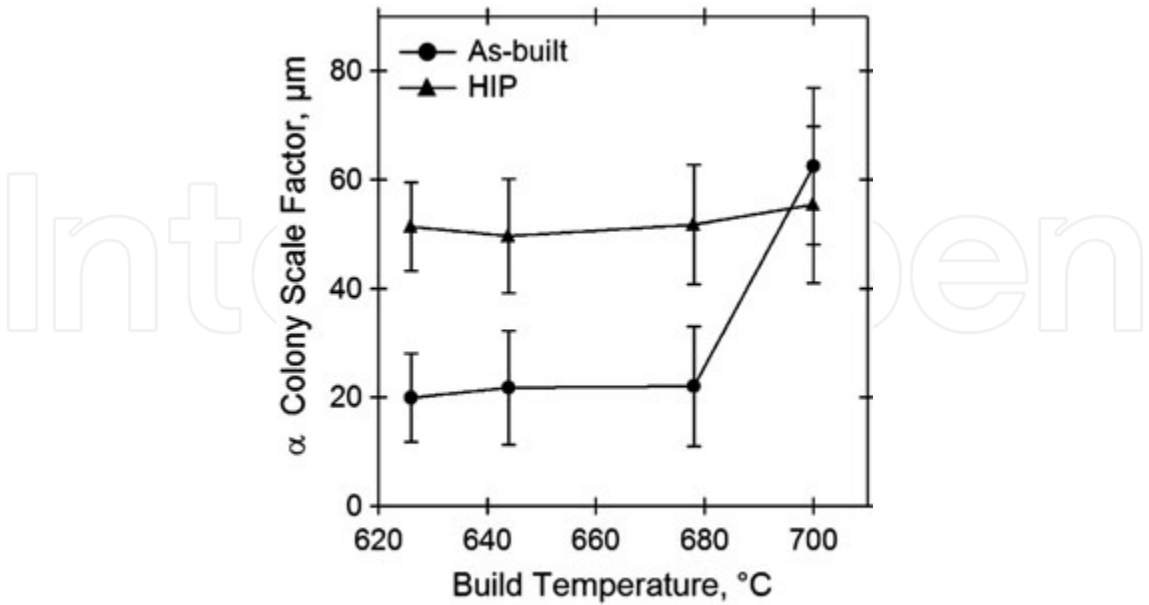
Figure 20. The size of the α colony in an SLS Ti-6Al-4V. HIP at (626°C-700°C) increases the α colony size evidently. HIP at higher temperatures can slightly increase the α colony size than those of lower temperatures [54].

# 8. Potential oxygen issue for the AM Ti-6Al-4V and counter measurements

8.1. Oxygen equivalent and oxygen level in AM Ti-6Al-4V

Oxygen is detrimental to ductility of Ti-6Al-4V especially when it exceeds certain level [97-99]. Miura et al. [26] suggests the critical oxygen level for PM Ti-6Al-4V is 0.33 wt.%, above which ductility drops rapidly and can be much lower than the corresponding ASTM specification (see Fig. 1b). It needs to be noted that C, N and Fe may affect the mechanical performance of Ti-6Al-4V in a similar way to that of the oxygen, as suggested by the following Eq. (3) [100] and Eq.(4) [101].

$$[O]_{EQ} = [O] + 2[N] + 2/3[C] \; (wt.\%) \tag{3}$$

$$[O]_{EQ} = [O] + 2.77[N] + 0.1[Fe] \; (wt.\%) \tag{4}$$

Generally speaking, AM processing only mildly increases oxygen level and the oxygen level in most of the as-built AM Ti-6Al-4V remain low [29-88]. This is mostly contributed to the extra-low interstitial (ELI) raw powders used, good vacuum condition and/or inert gas protection achievable during AM processing. Only occasional report can be found where oxygen level is higher than the 0.2 wt.%O benchmark value, see Figure 21 [29-88].
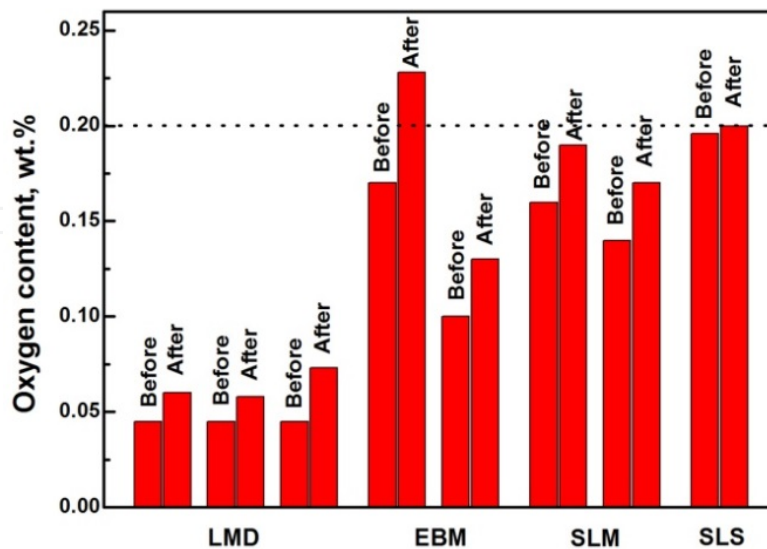

Figure 21. Variation of oxygen content before and after AM [29-88]. Dotted line in the figure represents corresponding ASTM specification (0.2 wt.%O).

8.2. Price issue of raw AM powders

Figure 21 indicates that the oxygen issue may have not been serious to the AM Ti-6Al-4V so far. This is mainly thanks to the use of ELI powders that are prepared by gas-atomisation or rotating electrode. The high cost of the ELI raw powders, however, can be an issue to AM Ti-6Al-4V from cost perspective. Figure 22 compares the price of a variety of powders, showing that the cost on the AM powders is extraordinary [4-13]. They are mostly higher than $400 per kg while hydrogenation-dehydrogenation (HDH) Ti powders that are widely used in conventional PM Ti are merely around $30 per kg. The high cost can be the bottle-neck issue for AM Ti-6Al-4V to be fully embraced by industries. For this reason, low-cost, high-interstitial (i.e. oxygen), fine powders are more desired for developing cost-effective AM Ti alloys. Sun et al. [102] recently developed an approach to manipulate irregularly-shaped HDH powders to make round-shaped, fine particles that are suitable for AM. The cost of their powders is higher than the HDH Ti powder but still markedly lower than the current AM powders, making it be more reliable for developing AM Ti and Ti alloys.
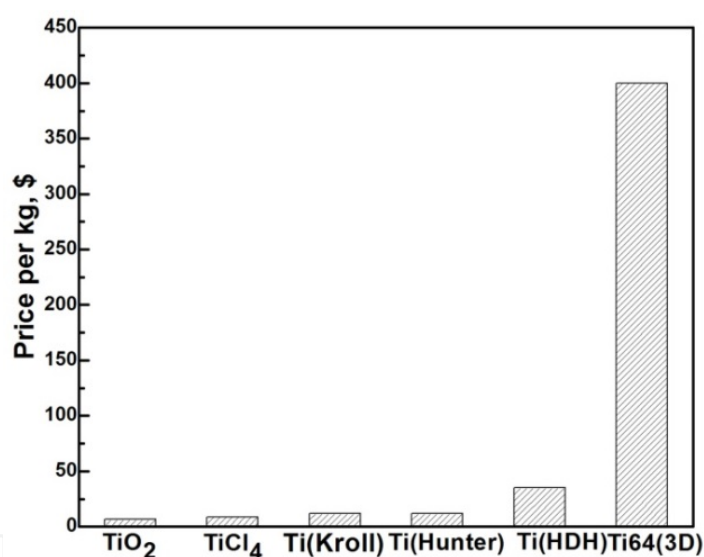
Figure 22. Comparison on the cost of various Ti materials, including raw material (TiO$_2$), intermediate material (TiCl$_4$) and Ti powders produced via the Kroll, Hunter and HDH approaches (price of Ti-6Al-4V is similar to these Ti powders). Price of fine powders of Ti-6Al-4V for the 3D printing is extraordinary [4-13].

8.3. Counter measurements

Counter measurements need to be consulted when the high impurity (oxygen) powders are to be used for developing AM Ti-6Al-4V. Research has shown that the RE elements are capable to scavenge oxygen and their oxygen scavenging capability follows this sequence: Y>Er>Dy>Tb>Gd (see Figure 23a) [103, 104]. The high potency of yttrium in scavenging oxygen from AM titanium alloys is demonstrated in Figure 23 (b), where the uniformly distributed Y$_2$O$_3$ dispersoids are resulted from an addition of 0.1 wt.%Y to an EBM titanium alloy [105].

RE hydrides such as YH_2 have been further demonstrated to be able to scavenge, aside from oxygen, Cl, another important impurity element to Ti materials, Fig. 24 [106,107].
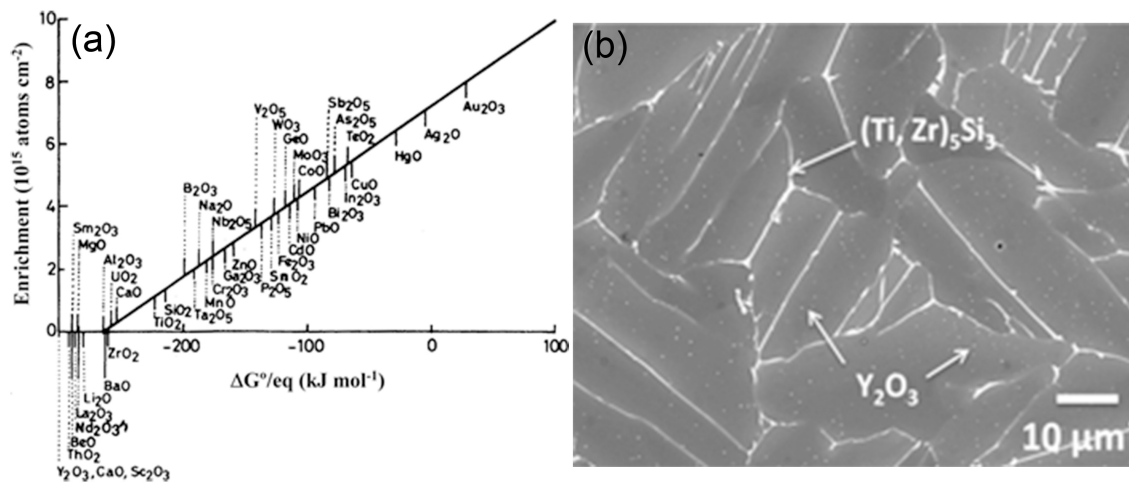
Figure 23. The free Gipps energy (ΔG) of formation of various oxide materials, showing their thermodynamic stability as well as their affinity for oxygen [104]. Rare earth elements such as Y and some alkaline earth elements such as Ca have higher affinity for oxygen than Ti. (b) Precipitation of fine Y_2O_3 dispersoids (due to the addition of 0.1 wt.%Y) in the α-Ti matrix of Ti-6Al-2.7Sn-4Zr-0.4Mo-0.45Si-0.1Y (wt.%) which contained 0.07 wt.% oxygen. The alloy was additively manufactured by EBM [105].
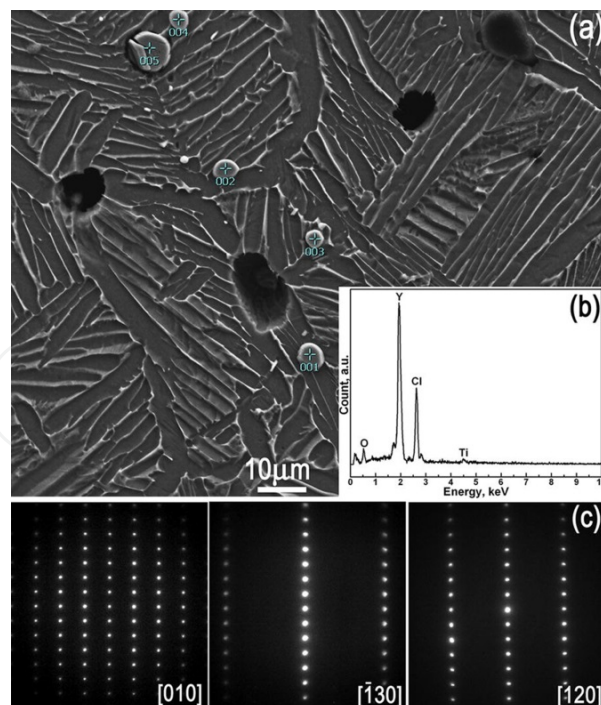
Figure 24. (a) SEM back-scatter-electron (BSE) image of Y-Cl particles in an YH_2-doped, as-sintered Ti alloy, (b) SEM energy dispersive x-ray (EDX) spectrum showing the enrichment of both Y and Cl in the phase and (c) TEM selected area electron diffraction (SAED) analysis of the phase [107].

9. Concluding remarks

3D printing has becoming a focusing topic not only to research community and industry but also to the general public, and AM Ti and Ti alloys is one of the most promising and interested areas to be further developed. For the time being, although a few issues persist such as the microstructural inhomogeneity in the as-built material, some of the AM Ti-6Al-4V have already been able to achieve mechanical properties no lower than the corresponding ASTM specifications. The cost of the ELI AM Ti powders is one of the most challenging issues to limit the scale-up of the AM products. Employing low-cost powders to replace existing expensive powders to reduce the overall cost is a valuable research direction for further developing AM Ti-6Al-4V. Counter measurements to deal with the impurity issue associated with the high-interstitial Ti powders can be one of the key research elements for such development.

Author details

Ming Yan[1,2*] and Peng Yu[2]

*Address all correspondence to: yan.m@sustc.edu.cn

1 RMIT University, School of Aerospace, Mechanical and Manufacturing and Centre of Additive Manufacture, Melbourne, VIC, Australia

2 The South University of Science and Technology, China

References

[1] Kobryn P A, Semiatin S L. The laser additive manufacture of Ti-6Al-4V. JOM, 2001, 53(9): 40-42.

[2] Chahine, G., Koike, M., Okabe, T., Smith, P., & Kovacevic, R. (2008). The design and production of Ti-6Al-4V ELI customized dental implants. JOM, 60(11), 50-55.

[3] Ivanova O, Williams C, Campbell T. Additive manufacturing (AM) and nanotechnology: promises and challenges. Rapid Prototyping Journal, 2013, 19(5): 353-364.

[4] Froes F H, Eylon D. Powder metallurgy of titanium alloys. International Materials Reviews, 1990, 35(1): 162-184.

[5] Imam M A, Froes F H S. Low cost titanium and developing applications. JOM, 2010, 62(5): 17-20.

[6] Qian, M. (2010). Cold compaction and sintering of titanium and its alloys for near-net-shape or preform fabrication. International journal of powder metallurgy, 46(5), 29-44.

[7] Ivasishin, O. M., Anokhin, V. M., Demidik, A. N., & Savvakin, D. G. (2000). Cost-effective blended elemental powder metallurgy of titanium alloys for transportation application. Key Engineering Materials, 188, 55-62.

[8] Qian, M., Yang, Y.F., Luo, S.D., Tang, H.P., Pressureless sintering of titanium and titanium alloys: sintering densification and solute hominization. In "Titanium Powder Metallurgy", (Editors) Qian, M., Froes, F.H. Elsevier and Science Direct, ISBN: 978-0-12-800054-0, in press, DOI: 10.1007/s11661-014-2631-4, 2014.

[9] Wang, Hongtao, Z. Zak Fang, and Pei Sun. A critical review of mechanical properties of powder metallurgy titanium. International journal of powder metallurgy 46, no. 5 (2010): 45-57.

[10] Yan, M., S. D. Luo, G. B. Schaffer, and M. Qian. TEM and XRD characterisation of commercially pure α-Ti made by powder metallurgy and casting. Materials Letters 72 (2012): 64-67.

[11] Yan, M., S. D. Luo, G. B. Schaffer, and M. Qian. Impurity (Fe, Cl, and P)-Induced Grain Boundary and Secondary Phases in Commercially Pure Titanium (CP-Ti). Metallurgical and Materials Transactions A 44, no. 8 (2013): 3961-3969.

[12] Yan, M., Qian, M., Kong, C., & Dargusch, M. S. (2014). Impacts of trace carbon on the microstructure of as-sintered biomedical Ti–15Mo alloy and reassessment of the maximum carbon limit. Acta biomaterialia, 10(2), 1014-1023.

[13] Yan, M., Dargusch, M.S., Kong, C., Kimpton, J., Kohara, S., Brandt, M., & Qian, M., In-situ synchrotron x-ray diffraction of the powder compacts of TiH$_2$-6Al-4V and Ti-6Al-4V: Accelerated alloying and phase transformation and the formation of an oxygen-enriched Ti$_4$Fe$_2$O phase in TiH$_2$-6Al-4V, Metallurgical and Materials Transactions A, in press, 2014.

[14] Leyens, C., & Peters, M. (2003). Titanium and titanium alloys (p. 187). Wiley-VCH, Weinheim.

[15] Lütjering, G., & Williams, J. C. (2003). Titanium (Vol. 2). Berlin: Springer

[16] Yang, Y. F., Imai, H., Kondoh, K., & Qian, M. (2014). Comparison of spark plasma sintering of elemental and master alloy powder mixes and prealloyed Ti-6Al-4V powder. International Journal of Powder Metallurgy, 50(1), 41-47.

[17] Lenel, F. V. (1980). Powder metallurgy: principles and applications (Vol. 225). Princeton, NJ: Metal Powder Industries Federation.

[18] German, R. M. (2005). Powder metallurgy & particulate materials processing (pp. 386-387). Princeton, NJ: Metal powder industries federation.

[19] Kingery, W. D., Bowen, H. K., & Uhlmann, D. R. Introduction to ceramics, 1976. New York, 788-1016.

[20] Crosby, K. D. (2013). Titanium-6Aluminum-4Vanadium for functionally graded orthopedic implant applications, Doctoral thesis, University of Connecticut.

[21] Robertson, I. M., & Schaffer, G. B. (2010). Comparison of sintering of titanium and titanium hydride powders. Powder Metallurgy, 53(1), 12-19.

[22] Fang, Z. Z., Sun, P., & Wang, H. (2012). Hydrogen Sintering of Titanium to Produce High Density Fine Grain Titanium Alloys. Advanced Engineering Materials, 14(6), 383-387.

[23] Li, S., Sun, B., Imai, H., & Kondoh, K. (2013). Powder metallurgy Ti–TiC metal matrix composites prepared by in situ reactive processing of Ti-VGCFs system. Carbon, 61, 216-228.

[24] Yan, M., Microstructural characterization of as-sintered Ti and Ti alloys. In "Titanium Powder Metallurgy", (Editors) Qian, M., Froes, F.H. Elsevier and Science Direct, ISBN: 978-0-12-800054-0, In press, 2014.

[25] Yan, M., M. S. Dargusch, T. Ebel, and M. Qian. A transmission electron microscopy and three-dimensional atom probe study of the oxygen-induced fine microstructural features in as-sintered Ti–6Al–4V and their impacts on ductility. Acta Materialia 68 (2014): 196-206.

[26] Miura, H., Itoh, Y., Ueamtsu, T., & Sato, K. (2010). The influence of density and oxygen content on the mechanical properties of injection molded Ti-6Al-4V alloys. Advances in Powder Metallurgy and Particulate Materials, 46-53.

[27] http://asm.matweb.com/search/SpecificMaterial.asp?bassnum=MTP641

[28] Elmer, J. W., Palmer, T. A., Babu, S. S., Zhang, W., & DebRoy, T. (2004). Phase transformation dynamics during welding of Ti–6Al–4V. Journal of applied physics, 95(12), 8327-8339.

[29] Roberts, I. A., Wang, C. J., Esterlein, R., Stanford, M., & Mynors, D. J. (2009). A three-dimensional finite element analysis of the temperature field during laser melting of metal powders in additive layer manufacturing. International Journal of Machine Tools and Manufacture, 49(12), 916-923.

[30] Facchini, L., Magalini, E., Robotti, P., Molinari, A., Höges, S., & Wissenbach, K. (2010). Ductility of a Ti-6Al-4V alloy produced by selective laser melting of prealloyed powders. Rapid Prototyping Journal, 16(6), 450-459.

[31] Thijs, L., Verhaeghe, F., Craeghs, T., Humbeeck, J. V., & Kruth, J. P. (2010). A study of the microstructural evolution during selective laser melting of Ti–6Al–4V. Acta Materialia, 58(9), 3303-3312.

[32] Vilaro, T., Colin, C., & Bartout, J. D. (2011). As-fabricated and heat-treated micro-structures of the Ti-6Al-4V alloy processed by selective laser melting. Metallurgical and Materials Transactions A, 42(10), 3190-3199.

[33] Knowles, C.R., Becker, T.H., Tait, R.B., Residual stress measurement and structural integrity implications for selective laser melted Ti-6Al-4V. South African Journal of Industrial Engineering, 2012, 23(3), 119-129.

[34] Pyka, G., Burakowski, A., Kerckhofs, G., Moesen, M., Van Bael, S., Schrooten, J., & Wevers, M. (2012). Surface modification of Ti6Al4V open porous structures produced by additive manufacturing. Advanced Engineering Materials, 14(6), 363-370.

[35] SU, X. B., YANG, Y. Q., YU, P., & SUN, J. F. (2012). Development of porous medical implant scaffolds via laser additive manufacturing. Transactions of Nonferrous Metals Society of China, 22, s181-s187.

[36] Lin, C. W., Ju, C. P., & Chern Lin, J. H. (2005). A comparison of the fatigue behavior of cast Ti–7.5 Mo with cp titanium, Ti–6Al–4V and Ti–13Nb–13Zr alloys. Biomaterials, 26(16), 2899-2907.

[37] Vrancken, B., Thijs, L., Kruth, J. P., & Van Humbeeck, J. (2012). Heat treatment of Ti6Al4V produced by Selective Laser Melting: Microstructure and mechanical properties. Journal of Alloys and Compounds, 541, 177-185.

[38] Leuders, S., Thöne, M., Riemer, A., Niendorf, T., Tröster, T., Richard, H. A., & Maier, H. J. (2013). On the mechanical behaviour of titanium alloy TiAl6V4 manufactured by selective laser melting: Fatigue resistance and crack growth performance. International Journal of Fatigue, 48, 300-307.

[39] Van Bael, S., Chai, Y. C., Truscello, S., Moesen, M., Kerckhofs, G., Van Oosterwyck, H.,... & Schrooten, J. (2012). The effect of pore geometry on the in vitro biological behavior of human periosteum-derived cells seeded on selective laser-melted Ti6Al4V bone scaffolds. Acta biomaterialia, 8(7), 2824-2834.

[40] Qiu, C., Adkins, N. J., & Attallah, M. M. (2013). Microstructure and tensile properties of selectively laser-melted and of HIPed laser-melted Ti–6Al–4V. Materials Science and Engineering: A, 578, 230-239.

[41] Pyka, G., Kerckhofs, G., Papantoniou, I., Speirs, M., Schrooten, J., & Wevers, M. (2013). Surface roughness and morphology customization of additive manufactured open porous Ti6Al4V structures. Materials, 6(10), 4737-4757.

[42] Chan, K. S., Koike, M., Mason, R. L., & Okabe, T. (2013). Fatigue Life of Titanium Alloys Fabricated by Additive Layer Manufacturing Techniques for Dental Implants. Metallurgical and Materials Transactions A, 44(2), 1010-1022.

[43] Amin Yavari, S., Wauthlé, R., van der Stok, J., Riemslag, A. C., Janssen, M., Mulier, M.,... & Zadpoor, A. A. (2013). Fatigue behavior of porous biomaterials manufactured using selective laser melting. Materials Science and Engineering: C, 33(8), 4849-4858.

[44] Rafi, H. K., Karthik, N. V., Gong, H., Starr, T. L., & Stucker, B. E. (2013). Microstructures and Mechanical Properties of Ti6Al4V Parts Fabricated by Selective Laser Melting and Electron Beam Melting. Journal of materials engineering and performance, 22(12), 3872-3883.

[45] Yadroitsev, I., Krakhmalev, P., & Yadroitsava, I. (2014). Selective laser melting of Ti6Al4V alloy for biomedical applications: Temperature monitoring and microstructural evolution. Journal of Alloys and Compounds, 583, 404-409.

[46] http://compolight.dti.dk/29509,2 (Courtesy of Olivier Jay)

[47] Nakamura, H., & Mitchell, A. (1992). The effect of beam oscillation rate on Al evaporation from a Ti-6Al-4V alloy in the electron beam melting process. ISIJ international, 32(5), 583-592.

[48] Zhuk, H. V., Kobryn, P. A., & Semiatin, S. L. (2007). Influence of heating and solidification conditions on the structure and surface quality of electron-beam melted Ti–6Al–4V ingots. Journal of materials processing technology, 190(1), 387-392.

[49] Kalinyuk, A. N., Trigub, N. P., Zamkov, V. N., Ivasishin, O. M., Markovsky, P. E., Teliovich, R. V., & Semiatin, S. L. (2003). Microstructure, texture, and mechanical properties of electron-beam melted Ti–6Al–4V. Materials Science and Engineering: A, 346(1), 178-188.

[50] Heinl, P., Müller, L., Körner, C., Singer, R. F., & Müller, F. A. (2008). Cellular Ti–6Al–4V structures with interconnected macro porosity for bone implants fabricated by selective electron beam melting. Acta biomaterialia, 4(5), 1536-1544.

[51] Facchini, L., Magalini, E., Robotti, P., & Molinari, A. (2009). Microstructure and mechanical properties of Ti-6Al-4V produced by electron beam melting of pre-alloyed powders. Rapid Prototyping Journal, 15(3), 171-178.

[52] Ponader, S., Von Wilmowsky, C., Widenmayer, M., Lutz, R., Heinl, P., Körner, C.,... & Schlegel, K. A. (2010). In vivo performance of selective electron beam-melted Ti-6Al-4V structures. Journal of biomedical materials research Part A, 92(1), 56-62.

[53] Murr, L. E., Gaytan, S. M., Medina, F., Martinez, E., Martinez, J. L., Hernandez, D. H.,... & Wicker, R. B. (2010). Characterization of Ti–6Al–4V open cellular foams fabricated by additive manufacturing using electron beam melting. Materials Science and Engineering: A, 527(7), 1861-1868.

[54] Al-Bermani, S. S., Blackmore, M. L., Zhang, W., & Todd, I. (2010). The Origin of Microstructural Diversity, Texture, and Mechanical Properties in Electron Beam Melted Ti-6Al-4V. Metallurgical and materials transactions a, 41(13), 3422-3434.

[55] Murr, L. E., Amato, K. N., Li, S. J., Tian, Y. X., Cheng, X. Y., Gaytan, S. M.,... & Wicker, R. B. (2011). Microstructure and mechanical properties of open-cellular biomaterials prototypes for total knee replacement implants fabricated by electron beam melting. Journal of the mechanical behavior of biomedical materials, 4(7), 1396-1411.

[56] Cronskär, M., Bäckström, M., & Rännar, L. E. (2013). Production of customized hip stem prostheses–a comparison between conventional machining and electron beam melting (EBM). Rapid Prototyping Journal, 19(5), 365-372.

[57] Li, S. J., Murr, L. E., Cheng, X. Y., Zhang, Z. B., Hao, Y. L., Yang, R.,... & Wicker, R. B. (2012). Compression fatigue behavior of Ti–6Al–4V mesh arrays fabricated by electron beam melting. Acta Materialia, 60(3), 793-802.

[58] Bush, R. W., & Brice, C. A. (2012). Elevated temperature characterization of electron beam freeform fabricated Ti–6Al–4V and dispersion strengthened Ti–8Al–1Er. Materials Science and Engineering: A, 554, 12-21.

[59] Cheng, X. Y., Li, S. J., Murr, L. E., Zhang, Z. B., Hao, Y. L., Yang, R.,... & Wicker, R. B. (2012). Compression deformation behavior of Ti–6Al–4V alloy with cellular structures fabricated by electron beam melting. Journal of the mechanical behavior of biomedical materials, 16, 153-162.

[60] Yang, L., Harrysson, O., West, H., & Cormier, D. (2012). Compressive properties of Ti–6Al–4V auxetic mesh structures made by electron beam melting. Acta Materialia, 60(8), 3370-3379.

[61] Safdar, A., Wei, L. Y., Snis, A., & Lai, Z. (2012). Evaluation of microstructural development in electron beam melted Ti-6Al-4V. Materials Characterization, 65, 8-15.

[62] Karlsson, J., Snis, A., Engqvist, H., & Lausmaa, J. (2013). Characterization and comparison of materials produced by Electron Beam Melting (EBM) of two different Ti–6Al–4V powder fractions. Journal of Materials Processing Technology, 213(12), 2109-2118.

[63] Antonysamy, A. A., Meyer, J., & Prangnell, P. B. (2013). Effect of build geometry on the β-grain structure and texture in additive manufacture of Ti6Al4V by selective electron beam melting. Materials Characterization, 84, 153-168.

[64] Hrabe, N., & Quinn, T. (2013). Effects of processing on microstructure and mechanical properties of a titanium alloy (Ti–6Al–4V) fabricated using electron beam melting (EBM), part 1: Distance from build plate and part size. Materials Science and Engineering: A, 573, 264-270.

[65] Hrabe, N., & Quinn, T. (2013). Effects of processing on microstructure and mechanical properties of a titanium alloy (Ti–6Al–4V) fabricated using electron beam melting (EBM), Part 2: Energy input, orientation, and location. Materials Science and Engineering: A, 573, 271-277.

[66] Schwerdtfeger, Jan, Robert F. Singer, and Carolin Körner. In situ flaw detection by IR-imaging during electron beam melting." Rapid Prototyping Journal 18, no. 4 (2012): 259-263.

[67] Banerjee, R., Collins, P. C., Genc, A., & Fraser, H. L. (2003). Direct laser deposition of in situ Ti–6Al–4V–TiB composites. Materials Science and Engineering: A, 358(1), 343-349.

[68] Miranda, R. M., Lopes, G., Quintino, L., Rodrigues, J. P., & Williams, S. (2008). Rapid prototyping with high power fiber lasers. Materials & Design, 29(10), 2072-2075.

[69] Brandl, E., Palm, F., Michailov, V., Viehweger, B., & Leyens, C. (2011). Mechanical properties of additive manufactured titanium (Ti–6Al–4V) blocks deposited by a solid-state laser and wire. Materials & Design, 32(10), 4665-4675.

[70] Brandl, E., Michailov, V., Viehweger, B., & Leyens, C. (2011). Deposition of Ti–6Al–4V using laser and wire, part I: Microstructural properties of single beads. Surface and Coatings Technology, 206(6), 1120-1129.

[71] Brandl, E., Michailov, V., Viehweger, B., & Leyens, C. (2011). Deposition of Ti–6Al–4V using laser and wire, part II: Hardness and dimensions of single beads. Surface and Coatings Technology, 206(6), 1130-1141.

[72] Baufeld, B., Brandl, E., & Van der Biest, O. (2011). Wire based additive layer manufacturing: comparison of microstructure and mechanical properties of Ti–6Al–4V components fabricated by laser-beam deposition and shaped metal deposition. Journal of Materials Processing Technology, 211(6), 1146-1158.

[73] Chen, J., Xue, L., & Wang, S. H. (2011). Experimental studies on process-induced morphological characteristics of macro-and microstructures in laser consolidated alloys. Journal of materials science, 46(17), 5859-5875.

[74] Ahsan, M. N., Pinkerton, A. J., Moat, R. J., & Shackleton, J. (2011). A comparative study of laser direct metal deposition characteristics using gas and plasma-atomized Ti–6Al–4V powders. Materials Science and Engineering: A, 528(25), 7648-7657.

[75] Brandl, E., Schoberth, A., & Leyens, C. (2012). Morphology, microstructure, and hardness of titanium (Ti-6Al-4V) blocks deposited by wire-feed additive layer manufacturing (ALM). Materials Science and Engineering: A, 532, 295-307.

[76] Brandl, E., & Greitemeier, D. (2012). Microstructure of additive layer manufactured Ti–6Al–4V after exceptional post heat treatments. Materials Letters, 81, 84-87.

[77] Clark, D., Whittaker, M. T., & Bache, M. R. (2012). Microstructural characterization of a prototype titanium alloy structure processed via direct laser deposition (DLD). Metallurgical and Materials Transactions B, 43(2), 388-396.

[78] Das, M., Balla, V. K., Basu, D., Manna, I., Sampath Kumar, T. S., & Bandyopadhyay, A. (2012). Laser processing of in situ synthesized TiB–TiN-reinforced Ti6Al4V alloy coatings. Scripta Materialia, 66(8), 578-581.

[79] Das, S., Wohlert, M., Beaman, J. J., & Bourell, D. L. (1998). Producing metal parts with selective laser sintering/hot isostatic pressing. JoM, 50(12), 17-20.

[80] Das, S., Beama, J. J., Wohlert, M., & Bourell, D. L. (1998). Direct laser freeform fabrication of high performance metal components. Rapid Prototyping Journal, 4(3), 112-117.

[81] Das, S., Wohlert, M., Beaman, J. J., & Bourell, D. L. (1999). Processing of titanium net shapes by SLS/HIP. Materials & design, 20(2), 115-121.

[82] Ramosoeu, M. E., Chikwanda, H. K., Bolokang, A. S., Booysen, G., & Ngonda, T. N. (2010). Additive manufacturing: Characterization of TI-6AI-4V alloy intended for biomedical application.

[83] Bertol, L. S., Júnior, W. K., Silva, F. P. D., & Aumund-Kopp, C. (2010). Medical design: direct metal laser sintering of Ti–6Al–4V. Materials & Design, 31(8), 3982-3988.

[84] Salmi, M., Tuomi, J., Paloheimo, K. S., Björkstrand, R., Paloheimo, M., Salo, J.,... & Mäkitie, A. A. (2012). Patient-specific reconstruction with 3D modeling and DMLS additive manufacturing. Rapid Prototyping Journal, 18(3), 209-214.

[85] Cooper, D. E., Stanford, M., Kibble, K. A., & Gibbons, G. J. (2012). Additive manufacturing for product improvement at Red Bull Technology. Materials & Design, 41, 226-230.

[86] Witek, L., Marin, C., Granato, R., Bonfante, E. A., Campos, F., Bisinotto, J.,... & Coelho, P. G. (2012). Characterization and in vivo evaluation of laser sintered dental endosseous implants in dogs. Journal of Biomedical Materials Research Part B: Applied Biomaterials, 100(6), 1566-1573.

[87] Stübinger, S., Mosch, I., Robotti, P., Sidler, M., Klein, K., Ferguson, S. J., & Rechenberg, B. (2013). Histological and biomechanical analysis of porous additive manufactured implants made by direct metal laser sintering: A pilot study in sheep. Journal of Biomedical Materials Research Part B: Applied Biomaterials, 101(7), 1154-1163.

[88] http://en.wikipedia.org/wiki/Selective_laser_sintering

[89] German, R. M. (1996). Sintering theory and practice. Sintering Theory and Practice, by Randall M. German, pp. 568. ISBN 0-471-05786-X. Wiley-VCH, January 1996., 1.

[90] German, R. M., Suri, P., & Park, S. J. (2009). Review: liquid phase sintering. Journal of materials science, 44(1), 1-39.

[91] Malinov, S., W. Sha, and Z. Guo. Application of artificial neural network for prediction of time–temperature–transformation diagrams in titanium alloys. Materials Science and Engineering: A 283, no. 1 (2000): 1-10.

[92] Ahmed, T., and H. J. Rack. Phase transformations during cooling in α β titanium alloys. Materials Science and Engineering: A 243, no. 1 (1998): 206-211.

[93] Majdic, Mojda, and Giinter Ziegler. Effect of the Metastable Beta-Phase on Phase Transformations in the Ti Alloy TiAl6V4. Z. Metallkunde 64, no. 11 (1973): 751-758.

[94]   Lu, S.L., Qian, M., Yan, M., Tang, H.P, & StJohn, D. (2014) Unpublished materials.

[95]   Kar, S., T. Searles, E. Lee, G. B. Viswanathan, H. L. Fraser, J. Tiley, and R. Banerjee. Modeling the tensile properties in β-processed α/β Ti alloys. Metallurgical and Materials Transactions A 37, no. 3 (2006): 559-566.

[96]   Collins, P. C., B. Welk, T. Searles, J. Tiley, J. C. Russ, and H. L. Fraser. Development of methods for the quantification of microstructural features in α+β-processed α/β titanium alloys. Materials Science and Engineering: A 508, no. 1 (2009): 174-182.

[97]   Yan, M., Xu, W., Dargusch, M.S., Tang, H.P., Brand & M., Qian, M. (2014), Powder Metallurgy, 57, no.4(2014): 251-257.

[98]   Yan, M., M. S. Dargusch, T. Ebel, and M. Qian. A transmission electron microscopy and three-dimensional atom probe study of the oxygen-induced fine microstructural features in as-sintered Ti–6Al–4V and their impacts on ductility. Acta Materialia 68 (2014): 196-206.

[99]   Yan, M., Y. Liu, G. B. Schaffer, and M. Qian. In situ synchrotron radiation to understand the pathways for the scavenging of oxygen in commercially pure Ti and Ti–6Al–4V by yttrium hydride. Scripta Materialia 68, no. 1 (2013): 63-66.

[100] H.R. Ogden, R.L. Jaffee: The effects of carbon, oxygen, and nitrogen on the mechanical properties of titanium and titanium alloys, TML Report No 20 Battelle Memorial Institute, 1995.

[101] Soeda; Seiichi (Tokyo, JP), Fujii; Hideki (Futtsu, JP), Okano; Hiroyuki (Chigasaki, JP), Hanaki; Michio (Chigasaki, JP): US patent, No. 6063211, "High strength, high ductility titanium-alloy and process for producing the same", 2000.

[102] Sun, Y.Y., Gulizia, S., Oh, C.H., Doblin, C., Yang, Y.F., Qian, M. Unpublished data.

[103] Okabe, T. H., Hirota, K., Kasai, E., Saito, F., Waseda, Y., & Jacob, K. T. (1998). Thermodynamic properties of oxygen in RE–O (RE=Gd, Tb, Dy, Er) solid solutions. Journal of alloys and compounds, 279(2), 184-191.

[104] Thompson, G. E., Skeldon, P., Zhou, X., Shimizu, K., Habazaki, H., & Smith, C. J. E. (2003). Improving the performance of aerospace alloys. Aircraft Engineering and Aerospace Technology, 75(4), 372-379.

[105] Tang, H.P., & Qian, M. Unpublished data.

[106] Yan, M., Tang, H.P., Qian, M.. Scavangin of oxygen ad chlorine from powder metallurgy (PM) titanium and titanium alloys. In "Titanium Powder Metallurgy", (Editors) Qian, M., Froes, F.H. Elsevier and Science Direct, ISBN: 978-0-12-800054-0, In press, 2014.

[107] Yan, M., Y. Liu, Y. B. Liu, C. Kong, G. B. Schaffer, and M. Qian. Simultaneous gettering of oxygen and chlorine and homogenization of the β phase by rare earth hydride additions to a powder metallurgy Ti–2.25 Mo–1.5 Fe alloy. Scripta Materialia 67, no. 5 (2012): 491-494.